Classification: Physical Sciences: Engineering

Resonant Sensor Arrays for Wireless Characterization of Solvated Ions

Sadaf Charkhabi[a], Adam R. Carr[a], Jiahao Wu[a], Subhanwit Roy[b], Andee M. Beierle[a], Dustin K. Thomas[a], Nathan M. Neihart[b], and Nigel F. Reuel[a]*

[a]Department of Chemical and Biological Engineering, Iowa State University, Ames, IA, 50011

[b]Department of Electrical and Computer Engineering, Iowa State University, Ames, IA, 50011

*Corresponding Author - reuel@iastate.edu

Abstract

A low-cost, passive resonant sensor was developed for wireless detection and measurement of ionic compounds. The sensor was fabricated as an open-circuit, Archimedean spiral composed of copper on a flexible, polyimide substrate. The sensor is interrogated by a two-loop antenna connected to a vector network analyzer (VNA) to monitor the scattering parameter response of the sensor when exposed to varying ionic concentrations. The sensor response was defined in terms of the resonant frequency and the peak-to-peak amplitude of the transmission scattering parameter profile ($|S_{21}|$). Potassium chloride (KCl) solutions with concentrations in the range of 100 nM – 4.58 M were tested on nine resonators having different length and pitch sizes to study the effect of sensor geometry on its response to ion concentration. The resonant sensors demonstrated an ion-specific response, caused by the variations in the relative permittivity of the solution, which was also a function of the resonator geometry. A lumped circuit model, which fit the experimental data well, confirms signal transduction via change in solution permittivity. Also, a ternary ionic mixture (composed of potassium nitrate (KNO_3), ammonium nitrate (NH_4NO_3), and ammonium phosphate ($NH_4H_2PO_4$)) response surface was constructed by testing 21 mixture variations on three different sensor geometries and the phase and magnitude of scattering parameters were monitored. It was determined that the orthogonal responses presented by resonant sensor arrays can be used for quantifying levels of target ions in ternary mixtures. Applications of these arrays include measuring the concentration of key ions in bioreactors, human sweat, and agricultural waters.

Resonant sensor | Ion concentration | LCR sensor | Wireless | Resonant frequency

Significance

Ions, such as potassium, nitrate, ammonium, and phosphate, play a significant role in agricultural, industrial, and biological processes. Therefore, detection and quantification of these are important for monitoring and measuring soil health, water quality, and human health. There are many existing technologies for measuring ion concentrations in solutions, such as ion chromatography, spectrophotometric methods, and optical fiber sensors; however, a completely untethered (no wires), and passive (no battery) method capable of real-time reporting of ionic concentration in closed environments has not been developed. Herein, we demonstrate the ion-specific response of resonant sensor arrays using a panel of ions that are relevant to environmental and agricultural problems.

Introduction

Charged chemical species, ions, are the signaling logic of biological systems and ubiquitous in natural waterways, industrial processes, and energy systems. Detection of their presence and level is important for many processes, such as harmful nitrates in field-runoff water that lead to eutrophic conditions in downstream waterways and result in algae blooms (1, 2). Since ions play such significant roles in many systems, there have been several methods developed for accurate measurement of ion concentration in solutions since the early 1900s (3) including, but not limited to, spectrophotometric methods (4), photoluminescent probes (5), ion chromatography (6), and optical fiber sensors (7). The major challenges incorporated with these techniques are the need for expensive instruments and direct access to the solution.

Another common method for characterizing specific ions in a solvated (typically water) mixture is using ion-selective membrane electrodes (ISME) (8). The basic principle of ISMEs is

measuring the potential difference caused by the interactions between the targeted ion and the ionophore which is present in the selective membrane (9). ISMEs can be categorized based on the type of their membranes: Solid state, glass membrane, liquid membrane, and polymer membrane electrodes are the most common types (10). A polymer membrane electrode is composed of an ionophore kept in a stationary polymer matrix in the presence of an electrically neutral organic solution in the membrane (10, 11). The most successful ion analytes for these types of ISME sensors are K^+, Ca^{2+}, Cl^-, and $NO3^-$ (10). A few limitations of ISMEs are 1) the selectivity of custom membranes, 2) the requirement to have physical access to the solution (wired probe) and 3) the need for repeated calibration (every two hours for precise measurement) (12).

In recent years, there have been some novel advances to ion concentration measurements. For instance, inkjet-printed graphene (IPG) can be used to make low-cost, solid-state ISME. In one work, a potassium-selective membrane was cast on an IPG electrode which rendered the sensor selective to potassium ions in the presence of competitive ions. These graphene-based sensors have an improved capability for ion sensing compared to the traditional electrochemical sensors due to graphene's properties such as high electron mobility (13). Other advances include coupling a solid-state ISME to powered, integrated circuits (ICs) that enable wireless measurement (*e.g.* Bluetooth, cellular) (14). Optical probes have also been developed to enable contact-free measurement, but require a transparent line of sight (15, 16). Measuring ions, contact-free, from opaque closed systems (biological, manufacturing, and processing) without wireless communication ICs (typically powered) has not been demonstrated. A simple, passive, wireless system is critical for applications where the sensor is widely distributed to many measurement nodes (*e.g.* a farm field or large runoff and river system) or in applications that demand a disposable price point (*e.g.* single-use bioreactors (17–23) or sweat analytic wearables (24–28)). Ion monitoring is needed to measure, model, and control these systems.

The focus of this paper is to demonstrate the use of passive, resonant sensors for the wireless measurement of ions. Resonant sensors, also known as LCR sensors, are inexpensive simple circuits containing an inductor (L), capacitor (C), and inherent system resistance (R) (29). The sensor has a specific resonant response which will modulate by altering one or more of the above-mentioned circuit parameters. The applicability of these sensors in measuring physical (*e.g.* temperature, humidity, strain, and pressure) (30–33), chemical (*e.g.* pH) (34–36), and biological (*e.g*. bacterial growth, enzyme activity, and tissue characterization) (37–40) parameters have been reported. In terms of ions, the concentration of nitrate, sulfate, and phosphate ions was estimated in water sources via planar electromagnetic sensors (41–43). For instance, tethered LC resonators have been used to sense phosphate and nitrate in solutions by correlating the ion concentration to the transmission coefficient response behavior using a vector network analyzer (44). However, the sensor is not truly wireless, as it is directly connected to the VNA via coaxial cables. Hence, it is not appropriate for applications in which it is not possible to have direct access to the sensor.

To the best of our knowledge, a non-invasive, low-cost, wireless, and passive sensor capable of reporting real-time, ionic concentration in aqueous solutions has not been described. Herein we demonstrate the response of resonant sensors to a panel of ions that are relevant to environmental and agricultural applications. These sensors resonate at specific frequencies, which can be tuned by the resonator's geometry (29), and herein we show how these resonant properties are modulated based on the type and amount of solvated ions. To describe this

phenomenon, we also model the effect of ions using a lumped circuit model to validate the transduction mechanism proposed as a change in solution permittivity. Moreover, we experimentally determine the effect of resonator geometry on ion-specific response and finally show the limits of fingerprinting ternary mixtures of ionic compounds with an array of three resonators with orthogonal responses.

Results & Discussion

As explained in the previous works (31, 40), the resonators were rapidly fabricated in a standard laboratory without lithographic processes. In brief, the steps were: 1) depositing the spiral-shaped positive mask on a copper-polyimide flexible substrate, 2) etching the sheet to remove the unmasked copper, and 3) rinsing the sample with acetone to remove the mask (Fig. 1a). The resonator was then adhered to the base of a petri dish in order to prevent short-circuiting and the dish was securely positioned over a two-loop reader antenna connected to a vector network analyzer (VNA) (Fig. 1b). The VNA measures the scattering parameter (S parameters) from the system (phase and magnitude data). The sensing medium containing the ionic compound(s) of interest was added to the dish and the coupled signal from the LC sensor and medium was measured by the VNA. The dielectric properties of the sensor environment were affected by the ions in solution which resulted in variations in the reported values for the S-parameters. By monitoring the magnitude of the transmission S-parameter signal ($|S_{21}|$) over the frequency range of interest (10-100 MHz), we were able to extract two variables of the sigmoidal $|S_{21}|$ response (Fig. 1c): peak resonant frequency (I), and peak-to-peak amplitude (II). A custom algorithm is then used to detect the resonant (peak) and anti-resonant (trough) frequencies (red circles in Fig. 1c). The peak-to-peak amplitude is the vertical distance of the peak to trough, as a measure of power (dB) absorbed by the resonator.

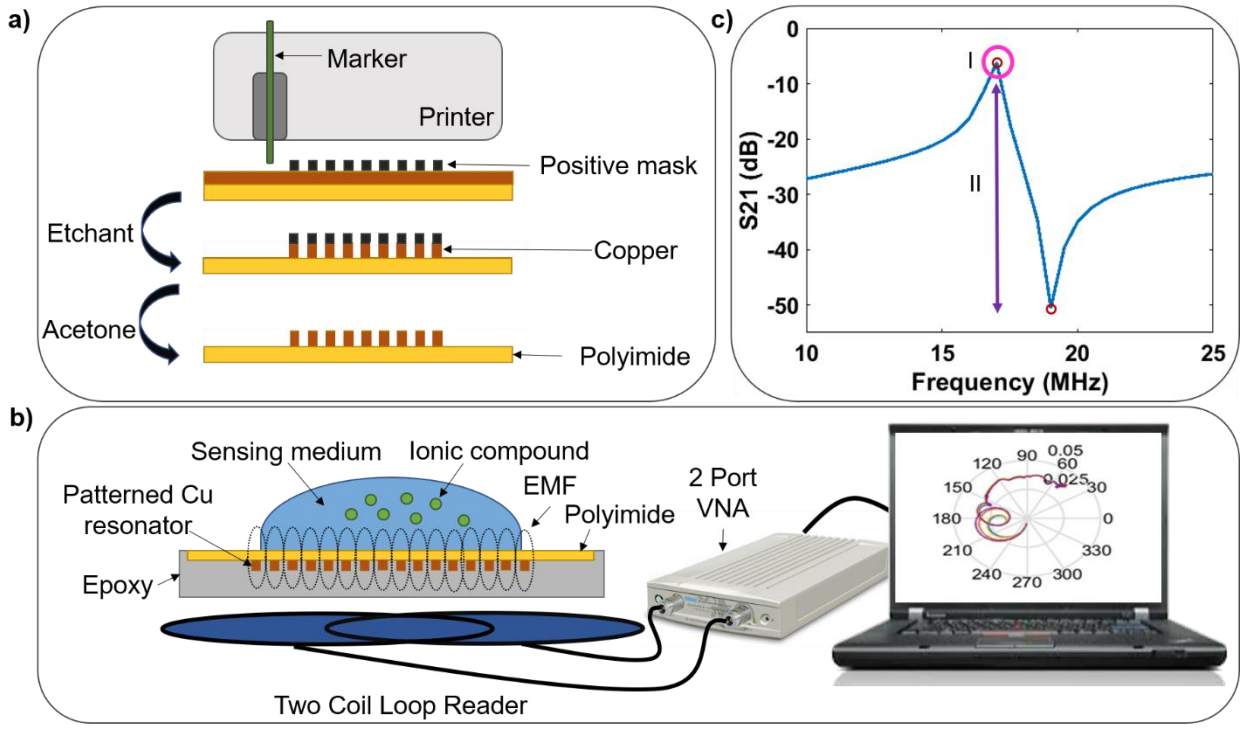

Figure. 1. Fabrication and operating principles of resonant sensors. a) Three-step process for prototyping resonant sensors from copper clad polyimide: positive masking, etching, and mask removal; b) summary of the method for detection and measurement of ionic compounds in a solution using an external reader antenna connected to a vector network analyzer and monitoring the scattering parameter response; c) example of the transmission magnitude response ($|S_{21}|$) in which resonant frequency and peak amplitude are noted as I and II, respectively.

Next, the response of the resonant sensor and reader antenna system were described with a lumped element model (Fig. 2a). Each non-concentric coil in the reader is modeled as a pair of coupled parallel LCR resonators where L_P models the self-inductance of each coil, C_P models the parasitic capacitance to ground, and R_P models the conduction losses in the reader. The coupling between each coil is modeled through the mutual inductance, M_1. The values for L_P, C_P, R_P, and M_1 were extracted from experimentally measured S-parameters from our system (168.8 nH, 9.4 pF, 27.3 kΩ, and -11.4 nH, respectively). The S-parameters were measured from 300 kHz to 100 MHz using an Agilent 5071C 4-port network analyzer calibrated such that the reference plane was at the terminals of the reader. While more complicated models could be used for the reader, good agreement between the simulated and measured S-parameters were obtained with the model (Fig. 2c and d).

The resonator is a spiral (Fig. 2b) of copper on a thin, flexible substrate, with its terminals left in an open circuit. The resonator has an outer diameter, d_{out}, an inner diameter, d_{in}, a pitch, P, and a set number of turns, N. Further, we define the average diameter and fill ratio to be:

$$d_{avg} = \frac{1}{2}(d_{out} + d_{in}) \qquad \text{(eq. 1)}$$

$$\rho = \frac{d_{out} - d_{in}}{d_{out} + d_{in}} \qquad \text{(eq. 2)}$$

Moreover, the material to which the resonator is exposed has a complex relative permittivity, ε_r. In our setup, this is the aqueous solution with ions above the resonator. The resonator (Fig. 2b) is modeled using a series LCR circuit (Fig. 2a), where the inductor, L_{res}, models the self-inductance of the resonator coil and R_{res} models the conduction losses in the metal. The capacitor, C_{res}, models the parasitic capacitance seen across the terminals of the resonator and is dependent upon the material to which the resonator is exposed. Finally, the interaction between the resonator and the reader is modeled with the mutual inductances M_{2A} and M_{2B}. The self-inductance of the resonator can be approximated using the following expression: (45)

$$L_{res} = \frac{1}{2}\mu_0 N^2 d_{avg}\left(\ln\left(\frac{2.46}{\rho}\right) + 0.2\rho^2\right) \qquad \text{(eq. 3)}$$

Where μ_0 is the permeability of free space (1.257×10^{-6} H/m), N is the number of turns, and d_{avg} and ρ are defined in (eq. 1) and (eq. 2), respectively. The value for the capacitor, C_{res}, is obtained from the self-resonant frequency, f_{SR}, of the resonator:

$$C_{res} = (4\pi^2 f_{SR}^2 L_{res})^{-1} \qquad \text{(eq. 4)}$$

The self-resonant frequency of the resonator will depend on the material to which the resonator is exposed through a change in the complex relative permittivity, ε_r. Using expressions adapted from (46), we can approximate the self-resonant frequency as:

$$f_{SR} = \frac{c}{2l\sqrt{\varepsilon_r}}(0.24N^{-0.46} + 0.95)(1 + \beta) \quad \text{(eq. 5)}$$

where c is the speed of light in free space, l is the total length of copper used to construct the resonator, and β is expressed as:

$$\beta = -\left((0.29 + 0.043\rho)\left(\frac{d_{in}}{d_{out}}\right) + 0.22\right)\left((\rho - 0.5)\left(2.65\left(\frac{P}{d_{out}}\right) + 0.03\right) + 1\right) \quad \text{(eq. 6)}$$

The series resistance of the resonator, R_{res}, is approximated from the resistivity of copper and the skin effect (47). It is assumed that the metal used to realize the resonator has a circular cross-section with an effective area expressed as:

$$A_{eff} = D\pi\sqrt{\frac{1.678 \times 10^{-8}}{\pi\mu_0 f_{SR}}} \quad \text{(eq. 7)}$$

where D is the cross-sectional diameter of the copper trace. The result of (eq. 7) can then be used to express the total AC resistance of the resonator as:

$$R_{res} = \frac{1.678 \times 10^{-8}}{A_{eff}} \cdot l \quad \text{(eq. 8)}$$

To demonstrate the utility of this model, a resonator with d_{in} = 1.5 mm, d_{out} = 40 mm, P = 1 mm, N = 20, and l = 1255 mm is considered. Equations (eq. 3) – (eq. 8) are evaluated for the cases where the resonator is exposed to air, DI water, and a 3 mM solution of potassium chloride (KCl). The static relative permittivity (relative permittivity at DC) for air and DI water are ε_{rA} = 1 and ε_{rW} = 80.4, respectively (48). The static relative permittivity for the KCl solution was estimated to be ε_{rKCl} = 78.8 (49). The resulting resonator model values are shown in Table. S1. We also compared simulated S-parameters of the model to measured S-parameters for air and DI water (Fig. 2e) and the 3 mM solution of KCl (Fig. 2f).

Using the model (Fig. 2a), the simulated $|S_{21}|$ matches well with experimental results for air and DI water (Fig. 2e). There are, however, resonant peaks in the measured response at approximately 40 MHz and 60 MHz that are not captured by the simulation. These peaks are likely the result of higher-order interactions between the reader/resonator/solution system that were not captured in this model. Comparing the simulated and measured $|S_{21}|$ for the KCl solution, we see that the model accurately predicts the frequencies of the peaks and valleys, but the simulated magnitudes are several dB larger than the measured values. This is due to the method by which the resonator loss is modeled. The loss was modeled as just the AC loss in the conductors. There is possible additional loss due to the increased conductivity of the

solution resulting in energy loss caused by the interaction between the electric fields and the ions in the solution.

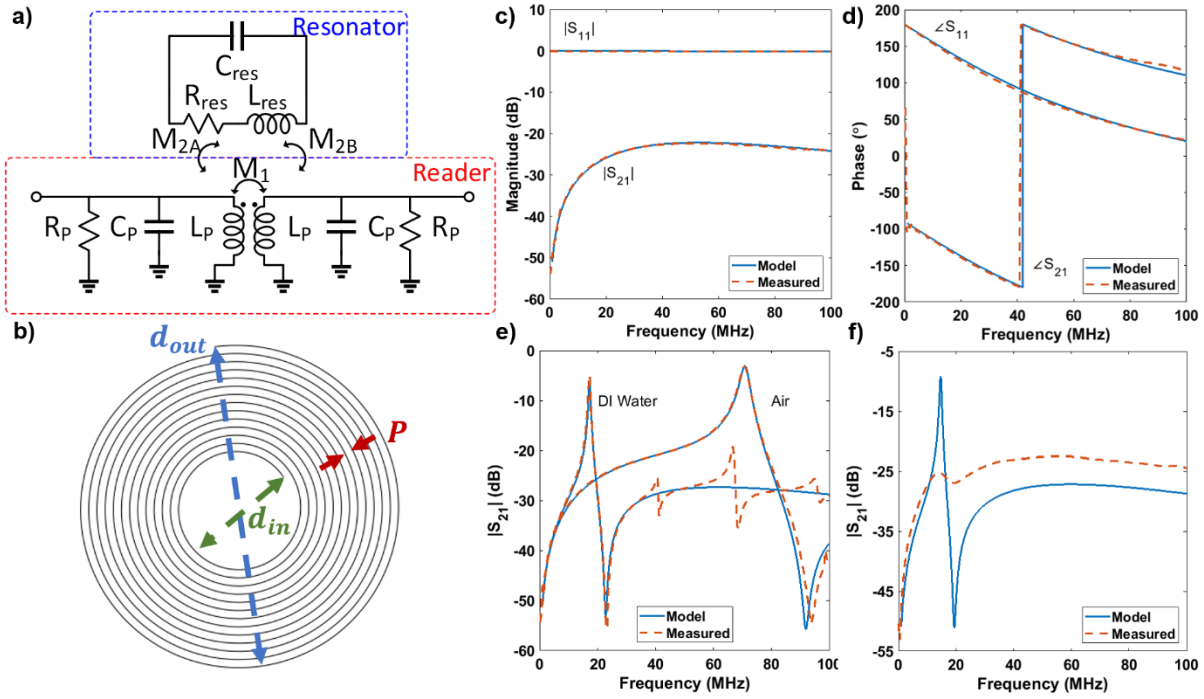

Figure. 2. Modeled response of the resonant circuit. a) Lumped circuit model of resonator and reader; b) the Archimedean spiral resonator having three design parameters: inner diameter, outer diameter, and pitch size; simulated and measured c) magnitude and d) phase of S_{21} and S_{11} for the reader; e) simulated and measured $|S_{21}|$ for the resonator exposed to air and DI water; f) Simulated and measured $|S_{21}|$ for 3 mM of KCl.

In order to determine the effect of the ion concentration existing in an aqueous solution on the $|S_{21}|$ response of the sensor, different concentrations of KCl, ranging from 100 nM to 1 M as well as the solubility limit of KCl in DI water at room temperature (4.58 M(50)), were measured on a resonator with d_{in} = 1.5 mm, d_{out} = 40 mm, P = 1 mm. To initialize the experiment, deionized (DI) water was initially added to the petri dish (50 ml) and the sensor setup was positioned at the center of the reader. Increasing concentrations of KCl were added to the solution while the total volume was kept constant in order to eliminate the effect of liquid volume on the sensor response. Using this method, 40 different concentrations of KCl were tested on the sensor (Table. S2). By monitoring $|S_{21}|$ (Code. S3), it was observed that the resonant frequency and amplitude change as a function of ion concentration (Fig. 3), however, not in a monotonic pattern as we expected.

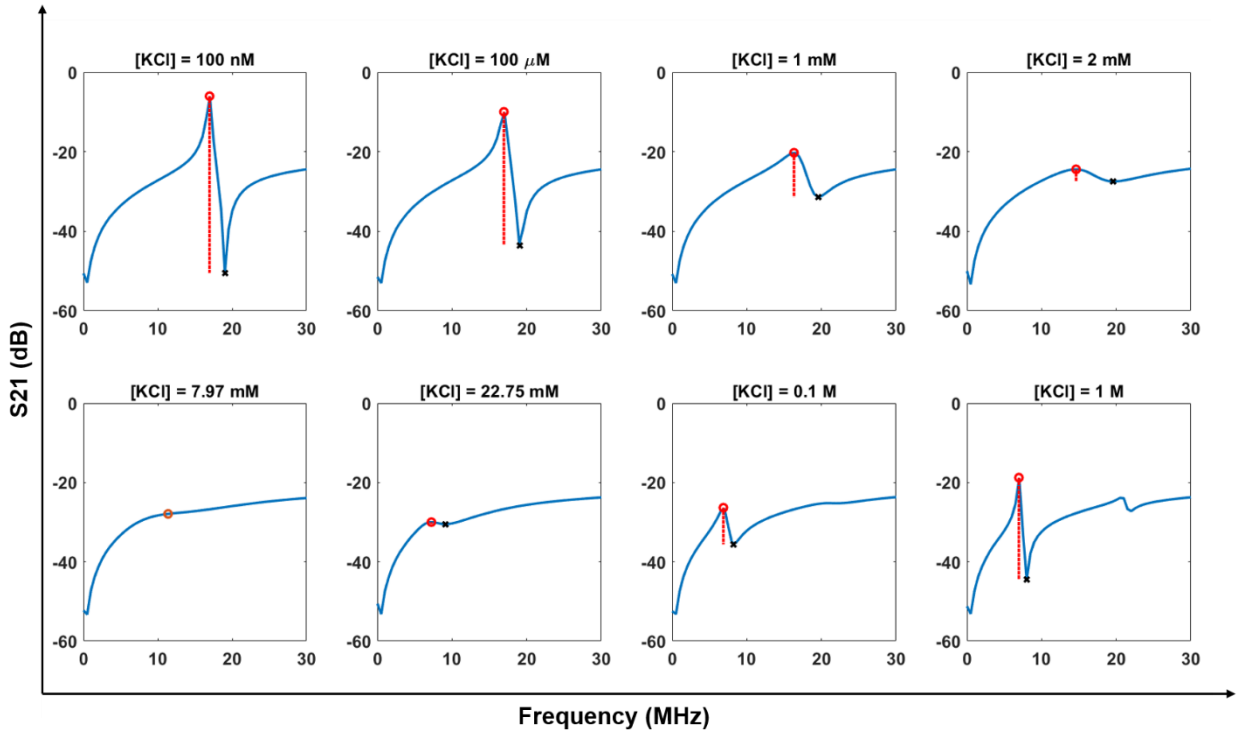

Figure. 3. $|S_{21}|$ (dB) response of 40mm diameter, 1mm pitch resonator to increasing concentration of KCl. Red circle denotes resonant peak, black x marks the anti-resonant trough, and the red dotted line shows peak amplitude.

The sensor response was more complex than anticipated (Video. S4). The resonant peak initially appeared (16.96 MHz for this sensor) and did not change with concentration from 0 to 0.1 mM KCl solution while the amplitude decreased. With further increase in the concentration of KCl, the resonant frequency shifted to a lower frequency (6.9 MHz) and it went through a transition point in where the peak was not detectable at 5 mM (amplitude of zero). Above 20 mM, the peak-to-peak amplitude increased, and the resonant frequency continued to decrease up to 60 mM and reached a relatively stable level again at higher concentrations. At this phase, the resonant frequency increased (0.174 MHz for the sensor in Fig. 3) as the concentration increased from 60 mM to 4.58 M.

As modeled above, there are three main circuit parameters affecting the system resonance: inductance (L), capacitance (C), and resistance (R). Based on Eq. 5, the resonant frequency is solely dependent on the complex relative permittivity (ε_r), as all other terms, such as the inductance (L_{res}) of the sensor and number of turns (N) are dictated by the resonator design and assumed to be constant (51). Hence, any shift observed in the resonant frequency is due to changes in the permittivity caused by modifying the ionic concentration of the solution above the resonator.

The permittivity of real materials is frequency-dependent, as molecules within the material exhibit a phase lag and damping to the imposed, external electromagnetic field. These components of phase and damping are presented mathematically as a complex number defined as (52):

$$\varepsilon_r = \varepsilon' - j\varepsilon'' \qquad \text{(eq. 9)}$$

Where ε' is the real component of permittivity, which represents the polarization of the sample under the influence of an external electric field and is related to the lag between the phase of the applied electric field and the electric flux density. ε'' is the imaginary component which measures damping or dispersion of energy by the dielectric. The imaginary component can also be expressed related to both the conductivity and frequency (53):

$$\varepsilon'' = \varepsilon_d''(f) + \frac{\sigma}{2\pi f \varepsilon_0} \qquad \text{(eq. 10)}$$

where $\varepsilon_d''(f)$ represents the dipolar loss, σ is the DC conductivity, and ε_0 is the absolute permittivity of free space. Typically, for the solutions and ions of interest in this work, $\varepsilon_d''(f)$ is constant with concentration and becomes negligible at low frequencies (54).

In general, it is believed that higher salt concentration would increase the conductivity of the solution; however, the collisions of the ions with other particles present in the solution (e.g. water molecules, other ions, contaminations, etc.) constrain the ion movement (55). Hence, although all saline solutions are electrically conductive, their conductivity is a function of the amount of charge carried by the ions as well as how quickly their energy might disperse as heat.

At very low concentrations of KCl ($<10^{-4}$ M), there is not a significant dependence of permittivity on the concentration, as the solution is very dilute. Thus, the resonant frequency does not change (standard deviation of the measured resonant frequency for low concentrations of KCl is 0.008). For the concentration range of 0.1 mM to 60 mM, however, there is an observed, dramatic decrease in the resonant frequency; this is a function of changes in the relative permittivity of the medium in proximity and coupled to the resonator (eq. 5). Conversely, we observe a small increase in resonant frequency at higher concentrations, which would indicate a decrease in the relative permittivity for the higher salt levels.

There have been many efforts to study the behavior of permittivity as the salt concentration of a solution changes; however, we find varying results and reasoning in these different studies. A major challenge associated with measuring the relative permittivity of ionic solutions is due to their relatively large conductivities (56). In one theory it is concluded that for concentrations below 1M of a salt-water solution (*e.g.* potassium chloride, cesium chloride, and sodium chloride), the relative permittivity decreases with salt concentration (49, 57). This *dielectric decrement* phenomenon is attributed to the local electric field which is created by individual ions that inhibit the externally applied field (58). The water molecules have the propensity to align with the local electric fields generated by ions and a hydration shell is created around the ion. Therefore, the water molecules are less responsive to the externally applied field and the dielectric permittivity decreases. In another theory proposed by Little (56), it is hypothesized that each ion in the solution is surrounded by spherical shells of the solvent molecules. Furthermore, it is assumed that the relative permittivity does not change within the ordered region of the shell system. Also, the shell structure for both potassium and chloride are assumed to be similar since their mobilities in aqueous solutions are the same. As the K^+ and Cl^- approach each other and their outer shells come into contact (separation between the charges is 20^{o}A), a bridge of the directed solvent molecule will form which links the ions. Using these hypotheses, the total change in relative permittivity for dilute solutions is a parabolic function of KCl concentration governed by the following equation:

$$\delta\varepsilon = 34 \times 10^3[c]^2 - [370 + 6n_4][c] \quad \text{(eq. 11)}$$

In which n_4 is the number of effective molecules in the fourth shell, which is the outer shell since n_5 is assumed to be zero. The coefficients for $[c]^2$ and [c] are specified by the generation of dipole linkages and the shell structures, respectively. Therefore, the relative permittivity for potassium chloride would decrease to a minimum value with increasing the concentration but eventually increase to values higher than the value at zero concentration (~80). This general form is also confirmed via *force method* by Fürth (59) for sodium chloride and by Pechhold (60) for potassium, sodium, lithium, and hydrogen chloride. In another study conducted by Fürth regarding the relative permittivity of conducting liquids at low frequencies, increasing the concentration of the solution in the range of 2.5 – 10 mM caused an increase in the relative permittivity from 80.2 to 83 (61).

Another important theory about the relative permittivity of very dilute solutions (< 25 mM) was proposed through the Debye – Falkenhagen equation (eq. S5. 1 - 4) (62, 63) which can be simplified as:

$$\varepsilon_w - \varepsilon_{rw} = A\sqrt{\gamma^*} \quad \text{(eq. 12)}$$

In which ε_w is the relative permittivity of the solution at low frequencies (1-2 KHz), ε_{rw} is the relative permittivity of the solvent (80.4 for water), A is a constant which is dependent on the properties of the salt, such as ion mobilities, valency type, etc. (A = 3.76 for KCl) (Table S. 5). γ^* represents the equivalent concentration and is defined as a function of the number of positive and negative ions for each molecule (υ_i), the valency of the ion (z_i) and concentration of the solution ([c]):

$$\gamma^* = \upsilon_i z_i [c] \quad \text{(eq. 13)}$$

Although this study was validated for very low frequencies, the Debye and Falkenhagen theory was confirmed for frequencies up to 100 MHz, which is the frequency range in which our study was performed. Based on this equation, the relative permittivity should rapidly increase with concentration; however, it has been demonstrated that the agreement between the theoretical relative permittivity predicted by Debye – Falkenhagen and the experimental relative permittivity observed by Dunning and Shutt holds up to 2 mM (64). Based on these experimental data, for each salt, the relative permittivity of the aqueous solution can be calculated for concentrations less than 25 mM using (eq. 14):

$$\varepsilon_s - \varepsilon_{rw} = A\sqrt{\gamma^*} - \varepsilon_0\kappa\gamma^* + \varepsilon_0 K\gamma^{*2} \quad \text{(eq. 14)}$$

In which ε_s is the relative permittivity of the solution, $\kappa\gamma^*$ is correspondent to the Sack's factor (65) and κ is proportional to the square root of valencies of ions ($\sum z_i^{1/2}$) and its value is 0.74 for KCl. $K\gamma^{*2}$ factor is explained in terms of the desaturation effect (the number of saturation holes does not increase as rapidly as the concentration) and has a value of 16 for KCl. Hence, calculating the relative permittivity of KCl in terms of the concentration of the solution is possible using (eq. 15).

$$\varepsilon_s - \varepsilon_{rw} = 3.76\sqrt{\gamma^*} - 0.74\varepsilon_0\gamma^* + 16\varepsilon_0\gamma^{*2} \quad \text{(eq. 15)}$$

This equation has the capability to explain the decrease response of the resonant frequency (increase in the relative permittivity) for dilute solutions of KCl; however, the concentration range for which we observe this trend (0.1 mM – 60 mM) is larger than the one given by (eq.15) (up to 2 mM). The reason could be the same complexity we have observed in comparing previous studies, namely, generating a satisfactory equation to describe the behavior of relative permittivity for a large range of concentration is extremely challenging due to the high conductivity of the solution. Therefore, although explaining the effect of concentration on relative permittivity in terms of three separated phenomena of Debye-Falkenhagen (rise), Sack's factor (decrease), and desaturation (increase) helps with predicting the general trend, it is not able to fully predict the concentration ranges for which each theory holds.

Another phenomenon observed in the resonant frequency response is the small but not insignificant increase in the resonant frequency for the KCl concentration higher than 60 mM (standard deviation = 0.05), because of a decrease in the relative permittivity at high concentrations. This is attributed to the dipole saturation of the hydration shells around ions, which means the orientation polarizability of water molecules close to the ions decrease. This pattern has been observed before for high concentrations (e.g. 1 M) of strong electrolyte solutions, such as KCl, KNO_3, NaCl, etc. (66). Since the relative permittivity of the aqueous solution is determined by the polarization, it slightly decreases with increasing the concentration due to the dielectric saturation (>60 mM) (67). Although the above-mentioned theories all confirm the dielectric saturation of water in the vicinity of ions in the solution, discrepancies are observed regarding the concentration after which the saturation effect is not negligible. In the Dunning and Shutt theory, this critical concentration for KCl is about 5 mM (64), which is different from our experimental results (60 mM), likely due to the applicability of the available models.

Another important parameter extracted from the $|S_{21}|$ signal for all concentrations of KCl is the peak-to-peak amplitude. As mentioned earlier, as the concentration of KCl solution increases from 100 nM to ~10 mM, the peak-to-peak amplitude rapidly decreases, until it is not detectable anymore (peak-to-peak amplitude ~ 0 for concentration in the range of 10 – 17 mM). However, for concentrations higher than 17 mM, the peak-to-peak amplitude increases with concentration. Since the inductance of the resonator is assumed to be dependent on the physical parameters (e.g. length) of the spiral, it remains constant for all concentrations of KCl. Therefore, the changes in the peak-to-peak amplitude are attributed to the variations in the conductivity of the aqueous solution (68, 69). In order to describe the peak disappearance, first, it should be noted that with monitoring $|S_{21}|$ signal, we are in fact measuring the transmitted energy from one loop of the reader to the other. A disappearance in amplitude means that the energy sent by the VNA is being fully absorbed by the sensor/solution system. In other words, for KCl solutions with 10 – 17 mM concentration, there is a high energy loss due to an optimal impedance match and coupling to the sensor/solution system. This energy absorption is caused by the interaction between the electric field and ions in solution at these specific concentrations. The amplitude is zero through a range of concentrations. After this transition (KCl concentration > 17 mM), the energy loss to the sensor/solution system is again reduced and the transmission energy is again picked up by the second coil of the reader, and the resonant peak becomes detectable again.

Next, we determined the effect of resonator geometry on these $|S_{21}|$ responses (plotted using MATLAB (Code. S7)) caused by increasing KCl concentration. Nine resonators with variant pitch and length sizes were designed (Table. S6) and the same concentrations of KCl from above were studied. Similar patterns for shifts in resonant frequency and peak amplitude were observed (Fig. 4); however, the magnitudes of these measurements were dependent on the geometry of the sensor.

The initial resonant frequency (f_{SR}), which did not go through major changes up to 1mM, was observed to be dependent on the geometrical parameters (e.g. outer diameter, pitch size, number of turns, etc.) of the Archimedean spiral resonator. For resonators with similar length (1255 mm) and variant pitch sizes (1-2.5 mm), the measured self-resonant frequency was higher for a larger pitch size (Fig. S8a) which is consistent with the previous findings (37). For the spirals with a similar pitch size (1.2 mm) and different length (800-2764 mm), the resonant frequency was inversely related to the length size (Fig. S8b). As the length increases, both the outer diameter (d_{out}) and the number of turns (N) increase, which would cause the inductance (L_{res}) of the circuit to increase (Eq. 3). This causes a lower resonant frequency. For all geometries, the large decrease in resonant frequency was observed in the concentration range of 0.1 mM-0.1 M; however, the absolute value of this shift was more dependent on the length of the resonator rather than the pitch size (Fig. S9).

As mentioned earlier, the resonant frequency response to different concentrations of KCl can be explained through the electrical properties of ionic aqueous solutions theories. This trend is consistent through all the resonators; however, unexpectedly, the window in which the peak-to-peak amplitude is almost zero (*e.g.* where the resonator/solution system is most lossy) is dependent on the pitch size and coil length. We attribute this to the surface area of the sensor, which has the highest value for the largest pitch size and the largest coil length. For a resonator with a larger surface area, the reader antenna is better shielded from the ionic solution. Therefore the $|S_{21}|$ signal is less sensitive to the energy loss in this transition zone.

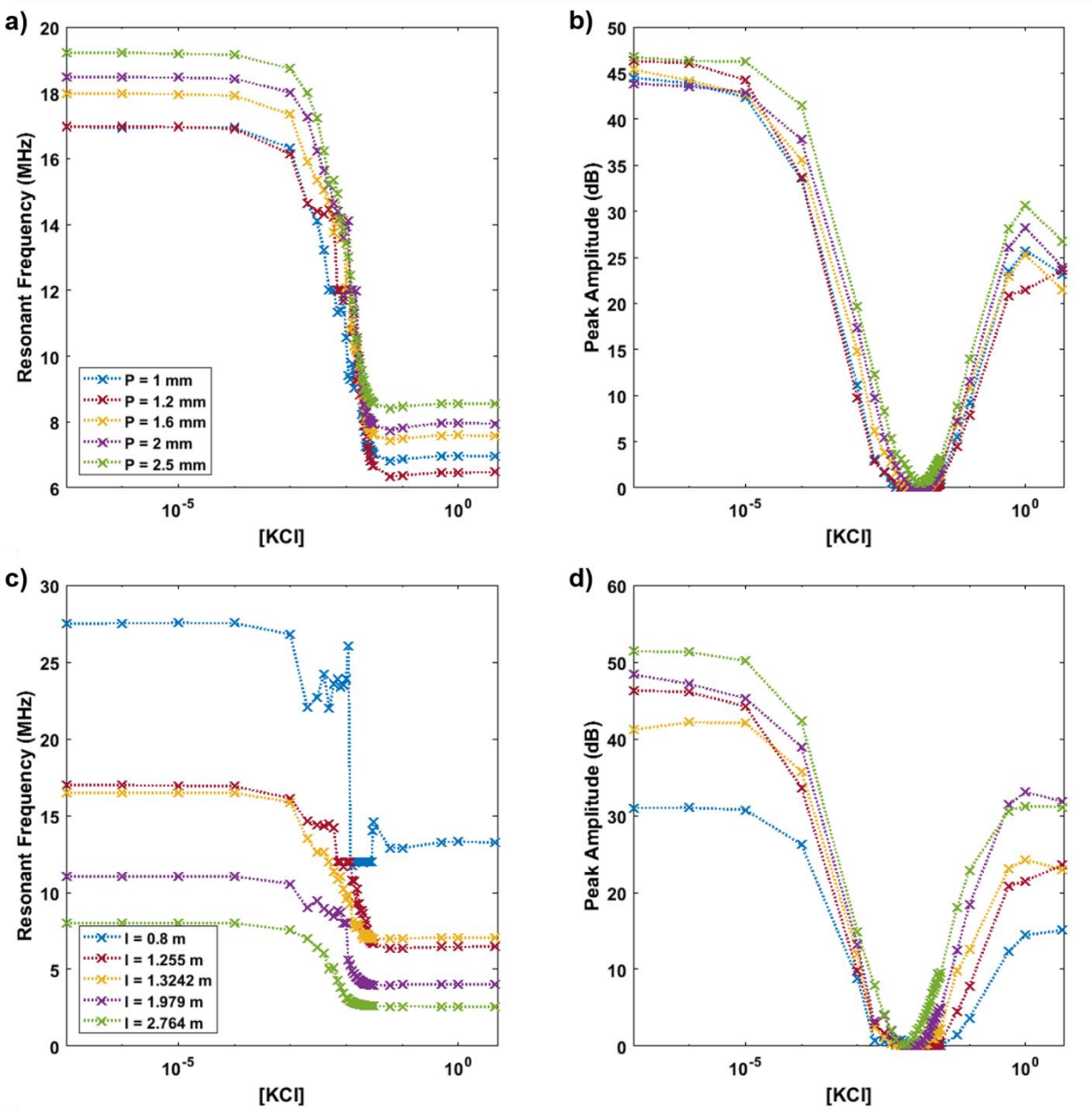

Figure. 4. Effect of resonator geometry on $|S_{21}|$ response to different concentration of KCl. The changes in resonant frequency and peak amplitude responses for resonators a-c) with 1.26 m spiral length with varying pitch and d-f) with constant 1.2 mm pitches and varying lengths (see Table S1).

To further study the sensor response to ionic compounds, four salts were chosen to be tested on resonators to investigate if the LC sensors have an ion-specific response. The salt panel included potassium nitrate (KNO_3), ammonium nitrate (NH_4NO_3), potassium phosphate (KH_2PO_4), and ammonium phosphate ($NH_4H_2PO_4$), which were carefully selected to have matched cation and anion pairs. Also, since nitrate and phosphate are among most important anions in agriculture, they were chosen to demonstrate the potential application of this work. Since the length of the resonator had a more significant effect on the changes in the resonant

frequency response to different KCl concentrations, three resonators with constant pitch size (1.2 mm) and different length (0.8, 1.26, and 2.76 m) were used for this test. The S_{21} sensor response for 100 µM, 2 mM, 30 mM, and 100mM for these salts are shown as polar plots (Fig. 5). Polar plots (Code. S10) are useful for these measurements as they show both the magnitude and phase of the S_{21} signal simultaneously, rather than just the magnitude data (Fig. 3 and 4) and subtle differences caused by geometric changes can be observed. In these polar plots, the radial gridlines represent the phase of S_{21} and the concentric circles demonstrate the radio frequency (RF) voltage gain (RF output voltage/RF input voltage), which can be calculated using $|S_{21}|$:

$$Voltage\ Gain = 10^{(|S21|/20)} \quad \text{(eq. 17)}$$

It was observed that the type of ion has a major effect on the sensor response for all concentrations of the ions and all geometries of the resonators (Video. S11). The reason that the sensor is able to have a unique response to each of these salts is that they have different polarization behavior which leads to different dielectric properties. Furthermore, the Debye – Falkenhagen expression (A) in (eq. 14) is dependent on the mobility of ions and the type of salt. Therefore, the relative permittivity of aqueous solutions is dependent on the solvated salt. Even for a concentration in the transition range (30 mM here) in which the resonator behavior might look independent of the type of salt due to the collapse of the amplitude, there are small variations observed. In general, the S_{21} signal response is more salt-dependent at very low (<10 mM) and very high (> 100 mM) due to the higher amplitude at these regions. Nonetheless, the salts with similar anion (KNO_3 - NH_4NO_3, and KH_2PO_4- $NH_4H_2PO_4$) result in a more similar sensor response. We attribute this to the potassium and ammonium having identical ionic mobilities of 1, while the ionic mobility for nitrate and phosphate are more unique, 0.972 and 0.45, respectively. Therefore, KNO_3 - NH_4NO_3, and KH_2PO_4- $NH_4H_2PO_4$ have similar electrical behavior in this system. Furthermore, it is of interest to note that the resonator having the smallest outer diameter has a more salt-specific response. We attribute this to the smaller shielding of the reader antenna associated with a smaller surface area of the Archimedean spiral resonator, which leads to a higher sensitivity of the sensor to the ionic solution and therefore, the variations between the sensor responses are easier to detect.

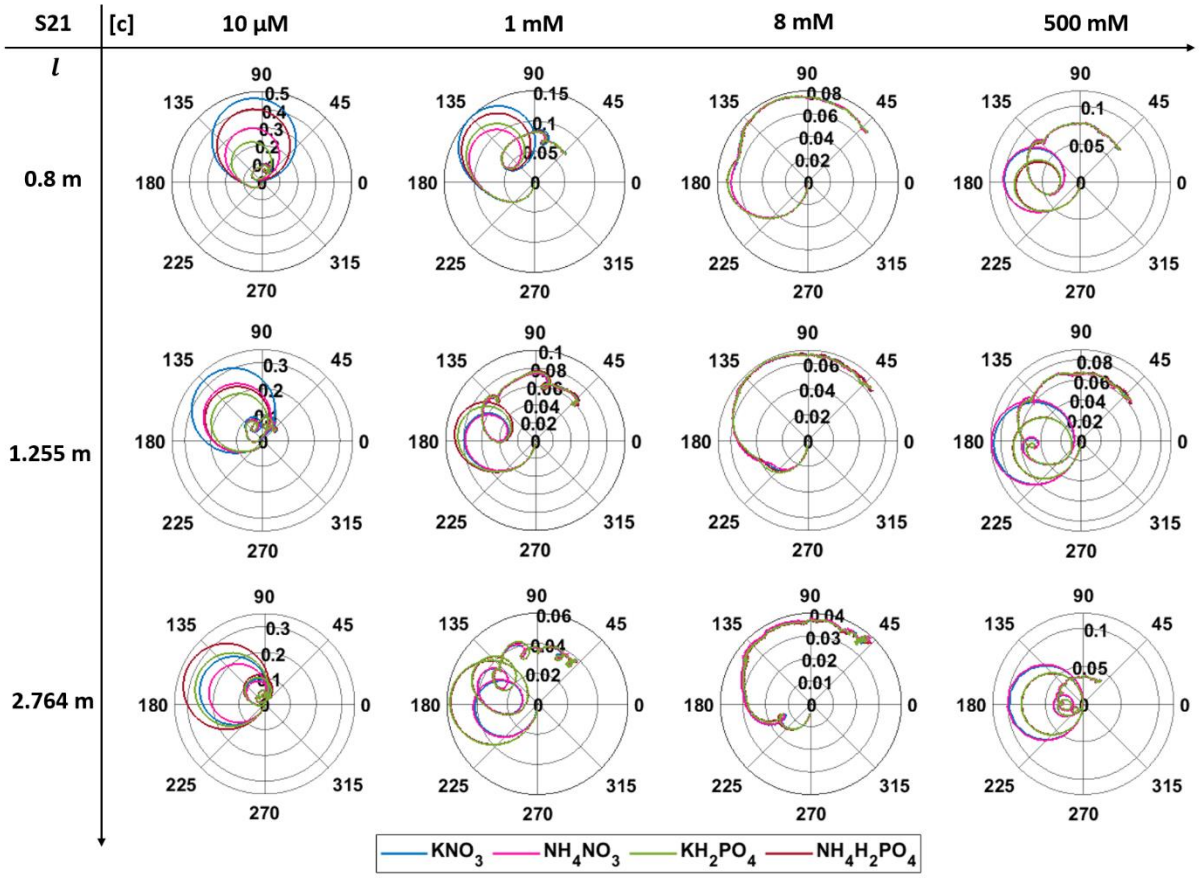

Figure. 5. Polar plots showing magnitude and phase of transmission scattering signal (S_{21}) for potassium nitrate (KNO_3), ammonium nitrate (NH_4NO_3), potassium phosphate (KH_2PO_4), and ammonium phosphate ($NH_4H_2PO_4$). The test was conducted using three resonators with 1.2 mm pitch size and varying length in the 100 nM – 1 M concentration range and the results are demonstrated here for four of these concentrations.

Observing that the sensor response was dependent on the concentration, type of ion, and resonator geometry, we then hypothesized that an array of resonators could provide orthogonal responses such that a mixture of ions could be differentiated to a certain degree. We tested this idea by preparing 21 samples of 1 mM solutions consisting of KNO_3, NH_4NO_3, and $NH_4H_2PO_4$ (Table. S12). The total ion concentration was kept constant at 1 mM in order to eliminate the effect of the concentration of the solution on the sensor response. Each individual salt component had a concentration ranging from 0 to1 mM. As mentioned earlier, changing the length of the Archimedean spiral resonator has a more significant effect on the resonant frequency shifts observed for different concentration values. Therefore, the three resonators used for this experiment had a 1.2 mm pitch size and 0.8, 1.225, and 2.764 m spiral length. The three parameters captured and plotted in ternary response diagrams (Code. S13) were $|S_{11}|$, $|S_{21}|$, and $\angle S_{21}$ (Fig. 6). For $|S_{21}|$, the magnitude was defined as the peak-to-peak amplitude as described earlier (Fig. S14 b). For the non-sigmoidal response of $|S_{11}|$ and $\angle S_{21}$ however, the results were reported in reference to the control solution (50 ml DI water) (Fig. S14a and c).

The ternary diagrams show that the resonator array responds with some orthogonality to different ion mixtures even though the total concentration of the solution is constant. The sensor response is dependent on the geometry of the resonator; however, the general trend (pattern of the ternary plot) of the response is consistent between different sensor sizes. Moreover, since KNO_3 and NH_4NO_3 are electrically similar (having cations with similar mobilities and identical anions), there is a relatively large region observed in the ternary plot in which modifying the concentration of KNO_3 and NH_4NO_3 does not cause a change on the scattering parameters; however, a major variation in the sensor response was observed by changing the $NH_4H_2PO_4$ concentration which we attribute to the sensor being more responsive to anion in this case due to the similar mobility of cations present in the solution (K^+ and NH_4). The ternary test was repeated in order to study the reproducibility of the sensor response and was found to be consistent (Fig. S15).

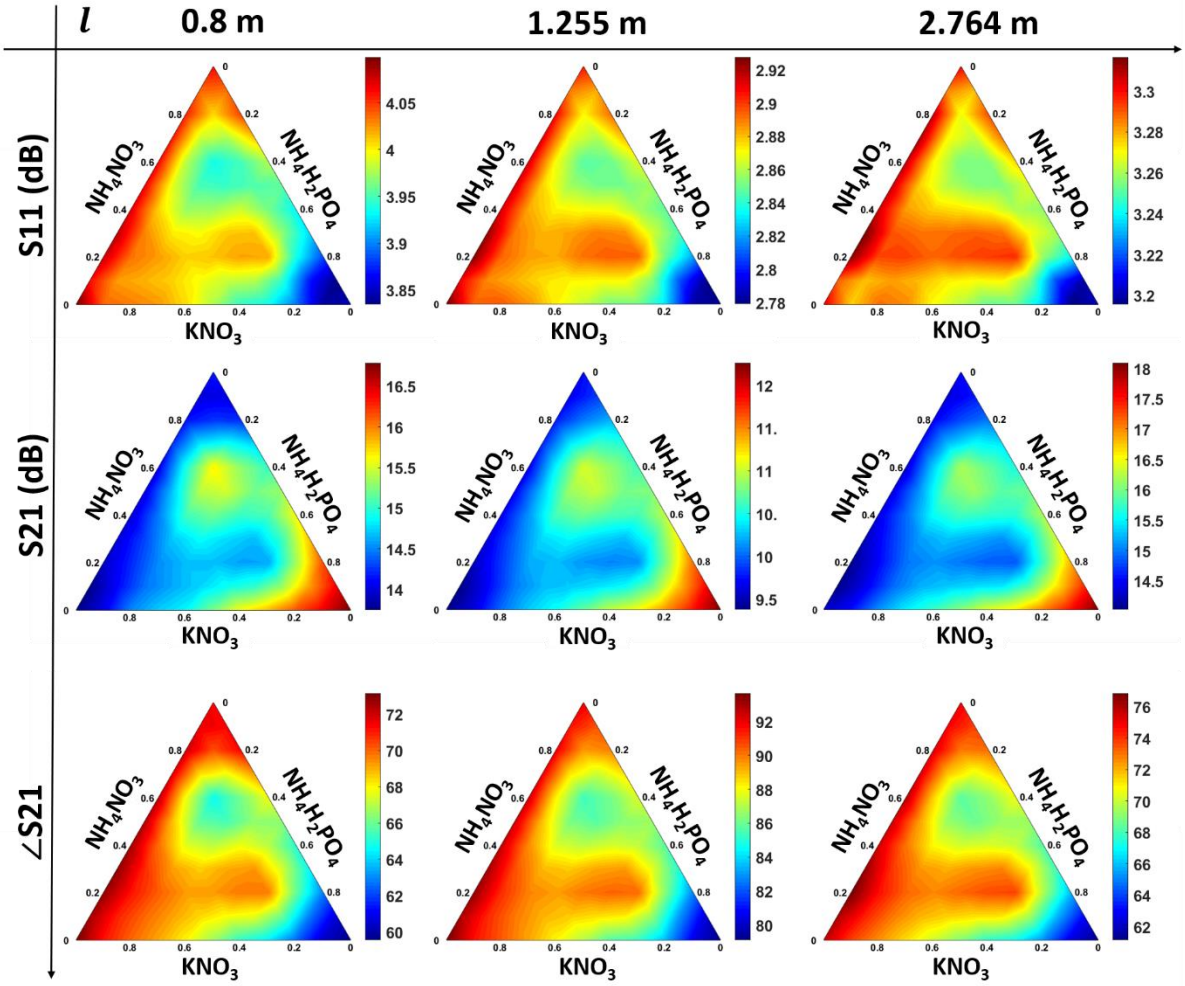

Figure. 6. The sensor response in terms of the magnitude of S_{11} (reflection signal) and magnitude and phase of S_{21} (transmission signal) to 1 mM solutions of various mixtures of KNO_3, NH_4NO_3, and $NH_4H_2PO_4$. The resonators used for this study were similar in pitch sizes (1.2 mm) and different in length size.

For all the sensor geometries and sensor response parameters, we observe four distinct regions observed in the ternary plots (Fig. 7a). As a final step, we tested the ability of the resonant sensor to be used for determining the concentrations of individual salts in a solution containing unknown concentrations of KNO_3, NH_4NO_3, and $NH_4H_2PO_4$. For this purpose, four 1 mM mixtures having unknown concentrations of the above-mentioned salts were prepared (Table. S16) and their $|S_{11}|$, $|S_{21}|$, and $\angle S_{21}$ were measured via the same three resonators used in the previous ternary mixture tests. We have developed an algorithm (Code. S17) to generate prediction regions of concentrations for the samples with unknown salt mixture, based on the ternary plots demonstrated in Fig. 6. The algorithm takes data collected from the unknown salt mixture and rank orders it with interpolated data from the ternary plots of the 21 known salt mixtures. The top percent (different for different regions based off of the size of the region) of points from this rank ordering are then plotted with the unknown point (Code. S17). It was observed that this algorithm is capable of predicting the dominant region to which the mixture belongs when the mixture is not on the borders between these regions (Fig 7d); however, we were not able to predict the exact values of the salt concentrations present in the solution (Fig. 7). This can be attributed to the quantity of the solutions (21 samples) used to create the interpolation map, this might not be sufficient for the predictions. Furthermore, we have only used three response parameters as the sensor response while we can extract eight scattering parameters ($|S_{11}|$ (dB), $\angle S_{11}$, $|S_{21}|$ (dB), $\angle S_{21}$, $|S_{12}|$ (dB), $\angle S_{12}$, $|S_{22}|$ (dB), and $\angle S_{22}$) for each sensor to make a prediction with higher accuracy. Also, using a larger sensor panel (e.g. 10 sensors) with different lengths might be helpful with determining the exact concentrations.

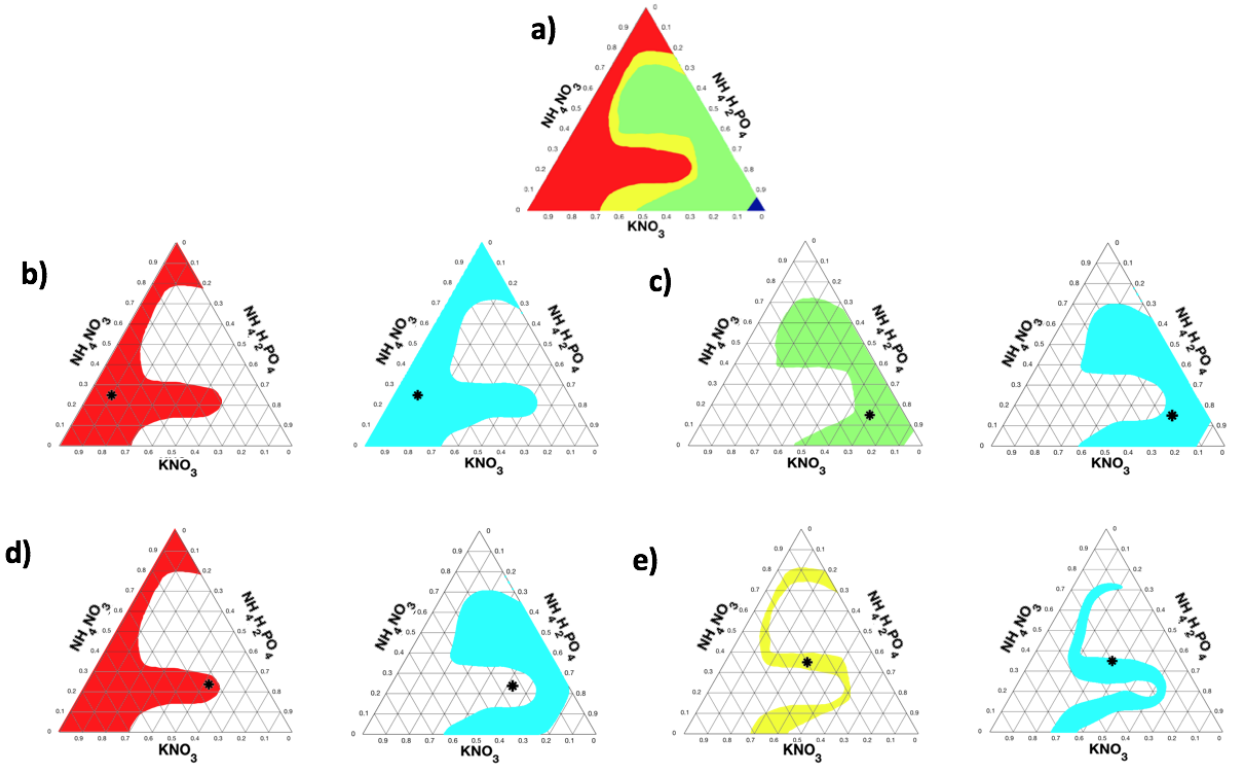

Figure. 7. Ternary mixture with unknown ionic concentration. (a) Concentration regions of ternary plots; (b), (c), (d), (e) Prediction region from (a) on left (red, yellow, green) and region predicted from ion predictor algorithm on right (cyan) for 1mM aqueous solutions containing different combinations of KNO_3, NH_4NO_3, and $NH_4H_2PO_4$ concentrations.

Conclusion

In this paper, we have demonstrated the fabrication of flexible and wireless resonant sensors to be used for the detection and quantification of ions in an aqueous solution. In this setup, the scattering parameter responses are captured using an external reader antenna connected to a benchtop vector network analyzer, which are further analyzed to extract the resonant frequency and peak-to-peak amplitude as the sensor response. We have also modeled the sensor and reader setup with a lumped element model, which closely matched the experimental data for air, DI water, and KCl media. Furthermore, KCl solutions having a concentration range of 0 – 1M as well as its solubility limit were tested on the wireless resonant sensor and the sensor showed a clear response to changes in the concentration. We attribute this response to a combination of Debye – Falkenhagen theory, Sack's effect, and desaturation effect. This response was similar for sensors with different geometrical features. Repeating the same test for KNO_3, NH_4NO_3, KH_2PO_4, and $NH_4H_2PO_4$, the sensor showed a salt-specific response, which was more dependent on the anion. The resonant sensor was then challenged in the presence of multiple salts and showed four clear concentration regions for all the responses. Finally, we were able to successfully predict the general concentration region of an unknown solution using an array of three resonators with different length sizes. This is the first demonstration of using an array of resonant sensors to attempt fingerprinting of ions in solution.

Future work includes improving the sensor selectivity and fabrication. We can potentially improve the sensitivity and selectivity of the sensor by using a larger array of resonators (>3 that were employed in this work) as well as attempting to leverage the ion-selective membranes (e.g. valinomycin for potassium (70)) as a coating on the resonator. Furthermore, the ability of the sensor array to accurately predict unknown ion concentrations can be fulfilled by testing more than 21 reference sample solutions, using more than three resonators, and extracting more than three scattering parameter features. This type of sensors has potential applications in industries for which measuring and detecting ions at low concentrations (<100 mM) is substantial such as biomedical and agricultural. This will especially become relevant when using other scalable fabrication methods, such as screen printing to make low-cost, single-use resonator arrays.

Materials and Methods

Fabrication of resonators and reading process. The spiral resonators were designed using Rhino 5 software and then transferred as a mask on copper coated polyimide via a Silhouette Curio XY plotter coupled to an ultrafine point permanent marker. The masked copper is placed in an etchant solution of 30 ml H_2O_2 and 15 ml HCl (37). The indelible ink was released from the sample by rinsing the sheet with acetone. As the final step, the resonator was inverted and sealed with epoxy to protect the coils from shorting. A coplanar two-loop reader antenna was connected to a vector network analyzer (VNA) to interrogate the resonator. The phase and the magnitude data of S_{21} and S_{11} were automatically recorded by a laptop using MATLAB. The resonant frequency and peak-to-peak amplitude of the resonant peak were determined with custom algorithms (Code. S3).

Ion concentration test procedure. To test the effect of ion concentration on the scattering parameter response, increasing concentrations of potassium chloride (KCl), potassium nitrate (KNO_3), monopotassium phosphate (KH_2PO4), ammonium phosphate ($NH_4H_2PO_4$), and ammonium nitrate (NH_4NO_3) were added to the resonator petri dish while the total liquid volume

was kept constant at 50ml. For this purpose, a panel of 40 different concentrations of the above-mentioned salts, ranging from 100 nM to their solubility limits in DI water at room temperature were tested on resonators with different geometries (Table. S2).

Ion mixture test. In order to study the ability of resonant sensors to have a specific response for different mixtures of ions, 21 samples containing different concentrations of KNO_3, $NH_4H_2PO_4$, and NH_4NO_3 were prepared which spanned the design space and allowed for the construction of ternary plots. The total concentration of each sample was kept at 1 mM and the volume was 25ml. These samples were tested on three resonators with constant pitch size (1.2 mm) and 0.8m, 1.255m, and 2.764m lengths and the magnitude and phase response of the S_{21} as well as the magnitude of the S_{11} were captured. Initially, the resonator of interest was fixed on the reader and then each sample was placed in the petri dish containing the resonator. After capturing the signal, the sample was removed, the sensor was completely cleaned without being moved, and the next sample was tested.

Unknown sample test. For each concentration region in the ion mixture ternary results, we prepared a sample called “mystery solution” or “unknown solution” in order to determine the concentrations of KNO_3, $NH_4H_2PO_4$, and NH_4NO_3 in the results of the ternary mixture test. The concentration information of these samples can be found in Table. S16. A linear interpolation was performed between the 21 points of the Ion mixture test using 150 majors in the “alchemyst/ternplotf” code for all data collected from three resonators with constant pitch size (1.2 mm) and 0.8m, 1.255m, and 2.764m lengths and the magnitude and phase response of the S_{21} as well as the magnitude of the S_{11}. The data collected from the “unknown solutions” were thank ranked ordered to the closest fit using least squared errors method.

Acknowledgments

Funding for this research was provided in part by NSF Industrial Innovation and Partnerships under award 1827578 and Iowa State University startup funds. The authors also thank DuPont for capital equipment donation.

References

1. Schindler DW, Vallentyne JR (2008) *The algal bowl: overfertilization of the world’s freshwaters and estuaries* (University of Alberta Press Edmonton).
2. Callisto M, Molozzi J, Barbosa JLE (2014) Eutrophication of Lakes BT - Eutrophication: Causes, Consequences and Control: Volume 2. eds Ansari AA, Gill SS (Springer Netherlands, Dordrecht), pp 55–71.
3. Buck RP, Lindner E (2001) Peer reviewed: tracing the history of selective ion sensors.
4. Narayana B, Sunil K (2009) A spectrophotometric method for the determination of nitrite and nitrate. *Eurasian J Anal Chem* 4(2):204–214.
5. Bai J, Zhang L, Liang R, Qiu J (2013) Graphene quantum dots combined with europium ions as photoluminescent probes for phosphate sensing. *Chem Eur J* 19(12):3822–3826.

6. Dudwadkar A, et al. (2013) Application of ion chromatography for the determination of nitrate in process streams of thermal denitration plant. *Sep Sci Technol* 48(16):2425–2430.

7. Ensafi AA, Amini M (2012) Highly selective optical nitrite sensor for food analysis based on Lauth's violet–triacetyl cellulose membrane film. *Food Chem* 132(3):1600–1606.

8. Ceresa A, Bakker E, Hattendorf B, Günther D, Pretsch E (2001) Potentiometric Polymeric Membrane Electrodes for Measurement of Environmental Samples at Trace Levels: New Requirements for Selectivities and Measuring Protocols, and Comparison with ICPMS. *Anal Chem* 73(2):343–351.

9. Pungor E, Horvai G (1994) *A Practical Guide to Instrumental Analysis* (Taylor & Francis) Available at: https://books.google.com/books?id=LMZ6NMaUT8AC.

10. Morf WE (2012) *The Principles of Ion-Selective Electrodes and of Membrane Transport* (Elsevier Science) Available at: https://books.google.com/books?id=UaY7AAAAQBAJ.

11. Bakker E, Bühlmann P, Pretsch E (1999) Polymer Membrane Ion-Selective Electrodes–What are the Limits? *Electroanal An Int J Devoted to Fundam Pract Asp Electroanal* 11(13):915–933.

12. Guide ISE Ion Selective Electrode Startup and Calibration Guide.

13. He Q, et al. (2017) Enabling Inkjet Printed Graphene for Ion Selective Electrodes with Postprint Thermal Annealing. *ACS Appl Mater Interfaces* 9(14):12719–12727.

14. Brennan Jr TM, et al. (2010) Influence of vertical sensor placement on data collection efficiency from bluetooth MAC address collection devices. *J Transp Eng* 136(12):1104–1109.

15. Kermis HR, Kostov Y, Harms P, Rao G (2002) Dual excitation ratiometric fluorescent pH sensor for noninvasive bioprocess monitoring: development and application. *Biotechnol Prog* 18(5):1047–1053.

16. Hirata T, et al. (2016) Protein-coupled fluorescent probe to visualize potassium ion transition on cellular membranes. *Anal Chem* 88(5):2693–2700.

17. Kusterer A, Krause C, Kaufmann K, Arnold M, Weuster-Botz D (2008) Fully automated single-use stirred-tank bioreactors for parallel microbial cultivations. *Bioprocess Biosyst Eng* 31(3):207–215.

18. Biechele P, Busse C, Solle D, Scheper T, Reardon K (2015) Sensor systems for bioprocess monitoring. *Eng Life Sci* 15(5):469–488.

19. Bluma A, et al. (2011) Process analytical sensors and image-based techniques for single-use bioreactors. *Eng Life Sci* 11(6):550–553.

20. Hillig F, Pilarek M, Junne S, Neubauer P (2013) Cultivation of marine microorganisms in single-use systems. *Disposable Bioreactors II* (Springer), pp 179–206.

21. Nurhayati RW, Ojima Y, Dohda T, Kino-Oka M (2018) Large-scale culture of a megakaryocytic progenitor cell line with a single-use bioreactor system. *Biotechnol Prog* 34(2):362–369.

22. Ahmed S, Chauhan VM, Ghaemmaghami AM, Aylott JW (2018) New generation of bioreactors that advance extracellular matrix modelling and tissue engineering. *Biotechnol Lett*:1–25.

23. Kessler M, Hoper J (1981) Ion-selective electrode device for polarographic measurement of oxygen.

24. Schazmann B, et al. (2010) A wearable electrochemical sensor for the real-time measurement of sweat sodium concentration. *Anal Methods* 2(4):342–348.

25. Curto VF, et al. (2012) Concept and development of an autonomous wearable micro-fluidic platform for real time pH sweat analysis. *Sensors Actuators B Chem* 175:263–270.

26. Wilhelm A, Wilhelm A, Emaminejad S (2018) Emerging wearable technologies for personalized health and performance monitoring. *Proc.SPIE*.

27. Coyle S, Diamond D (2016) Medical applications of smart textiles. *Advances in Smart Medical Textiles* (Elsevier), pp 215–237.

28. Coyle S, et al. (2009) Textile sensors to measure sweat pH and sweat-rate during exercise. *2009 3rd International Conference on Pervasive Computing Technologies for Healthcare* (IEEE), pp 1–6.

29. Charkhabi S (2018) Resonant sensors for passive, real-time, and wireless characterization of biological analytes.

30. Li C, et al. (2015) An Embedded Passive Resonant Sensor Using Frequency Diversity Technology for High- Temperature Wireless Measurement. 15(2):1055–1060.

31. Charkhabi S, et al. (2019) Kirigami-Enabled, Passive Resonant Sensors for Wireless Deformation Monitoring. *Adv Mater Technol*.

32. Ren QY, Wang LF, Huang JQ, Zhang C, Huang QA (2015) Simultaneous Remote Sensing of Temperature and Humidity by LC-Type Passive Wireless Sensors. *J Microelectromechanical Syst* 24(4):1117–1123.

33. Jia Y, Sun K, Agosto FJ, Quinones MT (2006) Design and characterization of a passive wireless strain sensor. *Meas Sci Technol* 17(11):2869.

34. Lei M, et al. (2004) A hydrogel-based wireless chemical sensor. *17th IEEE International Conference on Micro Electro Mechanical Systems. Maastricht MEMS 2004 Technical Digest* (IEEE), pp 391–394.

35. Cai QY, Grimes CA (2000) A remote query magnetoelastic pH sensor. *Sensors Actuators B Chem* 71(1–2):112–117.

36. García-Cantón J, Merlos A, Baldi A (2007) A wireless LC chemical sensor based on a high quality factor EIS capacitor. *Sensors Actuators, B Chem* 126(2):648–654.

37. Charkhabi S, Beierle A, McDaniel MD, Reuel NF (2018) Resonant Sensors for Low-Cost, Contact-Free Measurement of Hydrolytic Enzyme Activity in Closed Systems. *ACS Sensors*. doi:10.1021/acssensors.8b00267.

38. Ong KG, Bitler JS, Grimes CA, Puckett LG, Bachas LG (2002) Remote query resonant-circuit sensors for monitoring of bacteria growth: Application to food quality control. *Sensors* 2(6):219–232.

39. Yvanoff M, Venkataraman J (2009) A feasibility study of tissue characterization using LC sensors. *IEEE Trans Antennas Propag* 57(4):885–893.

40. Charkhabi S, Beierle A, Reuel N (2018) Short wave radio frequency resonators for transducing protein and cell surface interactions in closed systems. *ABSTRACTS OF PAPERS OF THE AMERICAN*

CHEMICAL SOCIETY (AMER CHEMICAL SOC 1155 16TH ST, NW, WASHINGTON, DC 20036 USA).

41. Nor ASM, Faramarzi M, Yunus MAM, Ibrahim S (2014) Nitrate and sulfate estimations in water sources using a planar electromagnetic sensor array and artificial neural network method. *IEEE Sens J* 15(1):497–504.

42. Yunus MAM, Mukhopadhyay SC (2010) Novel planar electromagnetic sensors for detection of nitrates and contamination in natural water sources. *IEEE Sens J* 11(6):1440–1447.

43. Gorji A, Bowler N (2018) Dielectric measurement of low-concentration aqueous solutions: assessment of uncertainty and ion-specific responses. *Meas Sci Technol* 29(8):85801.

44. Harnsoongnoen S, Wanthong A, Charoen-In U, Siritaratiwat A (2019) Microwave Sensor for Nitrate and Phosphate Concentration Sensing. *IEEE Sens J* 19(8):2950–2955.

45. Mohan SS, Hershenson M, Boyd SP, Lee TH (1999) Simple Accurate Expressions for Planar Spiral Inductances. 34(10):1419–1424.

46. Hooker JW, et al. (2015) An Empirical Expression to Predict the Resonant Frequencies of Archimedean Spirals. 63(7):2107–2114.

47. Tsuchiya A, Onodera H (2011) Gradient resistivity method for numerical evaluation of anomalous skin effect. *2011 IEEE 15th Workshop on Signal Propagation on Interconnects (SPI)* (IEEE), pp 139–142.

48. Topp GC (2003) State of the art of measuring soil water content. *Hydrol Process* 17(14):2993–2996.

49. Chen T, Hefter G, Buchner R (2003) Dielectric spectroscopy of aqueous solutions of KCl and CsCl. *J Phys Chem A* 107(20):4025–4031.

50. Pinho SP, Macedo EA (2005) Solubility of NaCl, NaBr, and KCl in water, methanol, ethanol, and their mixed solvents. *J Chem Eng Data* 50(1):29–32.

51. Andringa MM, Neikirk DP, Dickerson NP, Wood SL (2005) Unpowered wireless corrosion sensor for steel reinforced concrete. *SENSORS, 2005 IEEE* (IEEE), pp 4-pp.

52. Rishabh A (2012) *Wireless Communication* (S CHAND & Company Limited) Available at: https://books.google.com/books?id=XDJlDwAAQBAJ.

53. Roy S, Neihart NM, Bowler N (2018) Coaxial microwave resonant sensor design for monitoring ionic concentration in aqueous solutions. *2018 IEEE International Instrumentation and Measurement Technology Conference (I2MTC)*, pp 1–6.

54. Roy S (2017) Microwave resonant sensor for measurement of ionic concentration in aqueous solutions.

55. Seyfi S, Brown CS (2009) Apparatus and method for measuring salinity of a fluid by inductance.

56. Little VI (1955) The dielectric constant of aqueous ionic solutions. *Proc Phys Soc Sect B* 68(6):357.

57. Levy A, Andelman D, Orland H (2012) Dielectric constant of ionic solutions: A field-theory approach. *Phys Rev Lett* 108(22):227801.

58. Hasted JB, Ritson DM, Collie CH (1948) Dielectric properties of aqueous ionic solutions. Parts I

and II. *J Chem Phys* 16(1):1–21.

59. Furth R (1924) Dielektrizitatskonstanten Guter Leiter. *Phys Zeit* 25:676–679.

60. Pechhold R (1927) Untersuchung einiger wäßriger Elektrolytlösungen nach der Fürthschen Ellipsoidmethode. *Ann Phys* 388(11):427–456.

61. Bockris JO, Bowler-Reed J (1951) The measurement of dielectric constants of conducting liquids. *Br J Appl Phys* 2(3):74.

62. Anderson JE (1994) The Debye-Falkenhagen effect: experimental fact or friction? *J Non Cryst Solids* 172:1190–1194.

63. Falkenhagen H (1931) The principal ideas in the interionic attraction theory of strong electrolytes. *Rev Mod Phys* 3(3):412.

64. Dunning WJ, Shutt WJ (1938) The dielectric properties of aqueous solutions of salts. *Trans Faraday Soc* 34:467–479.

65. Hemmer PC (1996) *The Collected Works of Lars Onsager* (World Scientific) Available at: https://books.google.com/books?id=5wv3-WxzWJ4C.

66. Mollerup JM, Breil MP (2015) Modeling the permittivity of electrolyte solutions. *AIChE J* 61(9):2854–2860.

67. Wang C-C, Bruner LJ (1978) Dielectric saturation of the aqueous boundary layers adjacent to charged bilayer membranes. *J Membr Biol* 38(4):311–331.

68. Little VI, Smith V (1955) The Ionic Conductivity of Dilute Potassium Chloride Solutions at Centimetric Wavelengths. *Proc Phys Soc Sect B* 68(2):65.

69. Allison S, Wu H, Twahir U, Pei H (2010) Conductivity and electrophoretic mobility of dilute ionic solutions. *J Colloid Interface Sci* 352(1):1–10.

70. Eyal E, Rechnitz GA (1971) Mechanistic studies on the valinomycin-based potassium electrode. *Anal Chem* 43(8):1090–1093.

Figure Legends

Figure. 1. Fabrication and operating principles of resonant sensors. a) Three-step process for Prototyping of resonant sensor on Pyralux: positive masking, etching, and mask removal; b) summary of the method for detection and measurement of ionic compounds in a solution using an external reader antenna connected to a vector network analyzer and monitoring the scattering parameter response; c) example of the transmission magnitude response ($|S_{21}|$) in which resonant frequency and peak amplitude are noted as I and II, respectively.

Figure. 2. Modeled response of the resonant circuit. a) Lumped circuit model of resonator and reader; b) the Archimedean spiral resonator having three design parameters: inner diameter, outer diameter, and pitch size; simulated and measured c) magnitude and d) phase of S_{21} and S_{11} for the reader; e) simulated and measured $|S_{21}|$ for the resonator exposed to air and DI water; f) Simulated and measured $|S_{21}|$ for 3 mM of KCl.

Figure. 3. $|S_{21}|$ (dB) response of 40mm diameter, 1mm pitch resonator to increasing concentration of KCl. Red circle denotes resonant peak, black x marks the anti-resonant trough, and the red dotted line shows peak amplitude.

Figure. 4. Effect of resonator geometry on $|S_{21}|$ response to different concentration of KCl. The changes in resonant frequency and peak amplitude responses for resonators a-c) with 1.26 m antenna length with varying pitch and d-f) with constant 1.2mm pitches and varying lengths (see Table S1).

Figure. 5. Polar plots showing magnitude and phase of transmission scattering signal (S_{21}) for potassium nitrate (KNO_3), ammonium nitrate (NH_4NO_3), potassium phosphate (KH_2PO_4), and ammonium phosphate ($NH_4H_2PO_4$). The test was conducted using three resonators with 1.2 mm pitch size and varying length in the 100 nM – 1M concentration range and the results are demonstrated here for four of these concentrations.

Figure. 6. The sensor response in terms of the magnitude of S_{11} (reflection signal) and magnitude and phase of S_{21} (transmission signal) to 1 mM solutions of various mixtures of KNO_3, NH_4NO_3, and $NH_4H_2PO_4$. The resonators used for this study were similar in pitch sizes (1.2 mm) and different in length size.

Figure. 7. Ternary mixture with unknown ionic concentration. (a) Concentration regions of ternary plots; (b), (c), (d), (e) Prediction region from (a) on left (red, yellow, green) and region predicted from ion predictor algorithm on right (cyan) for 1mM aqueous solutions containing different combinations of KNO_3, NH_4NO_3, and $NH_4H_2PO_4$ concentrations.